



Void Replenishment: How Voids Accrete Matter Over Cosmic History

David Vallés-Pérez¹ , Vicent Quilis^{1,2} , and Susana Planellas^{1,2} ¹ Departament d'Astronomia i Astrofísica, Universitat de València. Burjassot (València), E-46100, Spain; david.valles-perez@uv.es² Observatori Astronòmic, Universitat de València. Paterna (València), E-46980, Spain

Received 2021 July 28; revised 2021 September 14; accepted 2021 September 16; published 2021 October 5

Abstract

Cosmic voids are underdense regions filling up most of the volume in the universe. They are expected to emerge in regions comprising negative initial density fluctuations, and subsequently expand as the matter around them collapses and forms walls, filaments, and clusters. We report results from the analysis of a cosmological simulation specially designed to accurately describe low-density regions, such as cosmic voids. Contrary to the common expectation, we find that voids also experience significant mass inflows over cosmic history. On average, 10% of the mass of voids in the sample at $z \sim 0$ is accreted from overdense regions, reaching values beyond 35% for a significant fraction of voids. More than half of the mass entering the voids lingers on periods of time ~ 10 Gyr well inside them, reaching inner radii. This would imply that part of the gas lying inside voids at a given time proceeds from overdense regions (e.g., clusters or filaments), where it could have been preprocessed, thus challenging the scenario of galaxy formation in voids, and dissenting from the idea of them being pristine environments.

Unified Astronomy Thesaurus concepts: Large-scale structure of the universe (902); Voids (1779); Accretion (14); Galaxy environments (2029); Computational astronomy (293)

Supporting material: animation

1. Introduction

Cosmic voids are underdense regions filling up most of the volume in the universe (Zeldovich et al. 1982). According to the accepted paradigm of cosmological structure formation, they emerge in regions comprising negative initial density fluctuations (Sheth & van de Weygaert 2004), and subsequently expand as the matter around them collapses and forms walls, filaments, and clusters (see van de Weygaert & Platen 2011 and van de Weygaert 2016 for recent, general reviews). This leads to coherent outflows (van de Weygaert & van Kampen 1993; Padilla et al. 2005; Ceccarelli et al. 2006; Patiri et al. 2012), making them a pristine environment with notable applications for cosmology (Dekel & Rees 1994; Park & Lee 2007; Lavaux & Wandelt 2010, 2012; Bos et al. 2012; Pisani et al. 2019) and galaxy formation (Hahn et al. 2007; Kreckel et al. 2011; van de Weygaert & Platen 2011; Ricciardelli et al. 2014a).

The dynamics of cosmic voids are dominated by their expansion and consequent depletion of gas and dark matter (DM), as revealed by the coherent outflows found both in simulations (van de Weygaert & van Kampen 1993; Padilla et al. 2005; Ceccarelli et al. 2006) and observations (Bothun et al. 1992; Patiri et al. 2012; Paz et al. 2013), and also expected from analytical models of isolated voids (Bertschinger 1985; Sheth & van de Weygaert 2004; Baushev 2021). However, in a fully cosmological environment, it should be in principle possible to expect coherent streams of matter—gas and DM—to unbind from dense structures and end up penetrating inside low-density regions. As a matter of fact, a handful of scenarios for unbinding mass do exist, such as galaxy cluster mergers (Behroozi et al. 2013) or strong shocks that can extend up to a few virial radii (e.g., Zhang et al. 2020).

In this Letter, we explore this scenario with a Λ cold dark matter (Λ CDM) cosmological simulation of a large volume domain, especially designed to describe matter in and around voids. The rest of the Letter is organized as follows. In Section 2, we describe the simulation and the void finding algorithm. In Section 3, we present our results regarding the existence of mass inflows through

voids' boundaries. Finally, we summarize the implications of these results in Section 4.

2. Methods

2.1. The Simulation

The results reported in this paper proceed from a cosmological simulation of a periodic domain, $100 h^{-1}$ Mpc along each direction, produced with MASCLET (Quilis 2004), an Eulerian, adaptive mesh refinement hydrodynamics coupled to a particle-mesh N -body code. The Eulerian hydrodynamic scheme in MASCLET, based on high-resolution shock-capturing techniques, is capable of providing a faithful description of the gaseous component in low-density regions, such as cosmic voids.

Structures evolve on top of a flat Λ CDM cosmology consistent with the latest Planck Collaboration (2020) results. Dark energy, matter, and baryon densities are specified by $\Omega_\Lambda = 0.69$, $\Omega_m = 0.31$, and $\Omega_b = 0.048$, relative to the critical density $\rho_c = \frac{3H_0^2}{8\pi G}$. The Hubble parameter, $H_0 = 100 h \text{ km s}^{-1} \text{ Mpc}^{-1}$, is set by $h = 0.678$. The initial conditions were set up at $z = 100$, by evolving a power spectrum realization with spectral index $n_s = 0.96$ and normalization $\sigma_8 = 0.82$ using Zeldovich's (1970) approximation.

A low-resolution run on a grid of 128^3 cells was performed in order to identify the regions that would evolve into cosmic voids by $z \simeq 0$. Back to the initial conditions, the seeds of voids and their surroundings were sampled with higher numerical resolution according to the procedure introduced in Ricciardelli et al. (2013, hereafter RQP13). The regions at $z = 100$ comprising the DM particles that end up in zones with³ $\rho/\rho_B < 10$ by $z = 0$ are thus mapped with a first level of mesh refinement ($\ell = 1$), with half the cell size and DM particles eight times lighter than those of the base grid; therefore, with

³ $\rho_B \equiv \Omega_m \rho_c$ is the background matter density of the universe.

DM mass resolution $6.4 \times 10^9 M_\odot$ and spatial resolution $390 h^{-1} \text{kpc}$. In order to capture the structures forming in cosmic voids, subsequent levels of refinement ($\ell \geq 2$, up to $n_\ell = 10$) are created following a pseudo-Lagrangian approach that refines cells where density has increased by a factor of 8 with respect to the previous, lower-resolution level. Besides gravity and hydrodynamics, the simulation includes standard cooling and heating mechanisms, and a phenomenological parameterization of star formation (Quilis et al. 2017).

2.2. The Void Finder

We have identified the sample of cosmic voids in our simulation with a void finder based on the one presented by RQP13, which looks for ellipsoidal voids using the total density field (ρ_{tot}) and the gas velocity field (\mathbf{v}), as underdense ($\rho_{\text{tot}} < \rho_B$), peculiarly expanding ($\nabla \cdot \mathbf{v} > 0$) regions surrounded by steep density gradients. While the original void finder in RQP13 did not assume any prior on the void’s shape, which could therefore develop highly complex, nonconvex, and non-simply connected shapes, such a precise definition of a void boundary is counterproductive for assessing mass fluxes in postprocessing, since it limits the validity of the pseudo-Lagrangian approach (see Section 2.3).

In order to have voids with smooth surfaces, our void finder looks for voids as ellipsoidal volumes around density minima, using the same thresholds on total density, total density gradient, and gas velocity divergence as RQP13. While voids are not generally ellipsoidal, by using the same threshold values as RQP13 we ensure that our algorithm looks for the largest possible ellipsoid inside actual, complex-shaped voids, thus providing a robust, stable, and conservative definition of these structures, which is readily comparable with their identification in observational data (Foster & Nelson 2009; Patiri et al. 2012). The voids are found and characterized one at a time, using the 128^3 base grid, in the steps summarized below.

Protovoid finding. A tentative center is chosen, as the most underdense, positive velocity divergence cell not yet inside an already found void. The initial protovoid is a 5^3 cells cube around this cell. The protovoid is then grown iteratively in the directions of its six faces, one extra cell along each direction at a time, if the following conditions are met by all the “new” cells:

$$\delta_{\text{tot}} < 0, \quad \nabla \delta_{\text{tot}} < (\nabla \delta)^{\text{max}}, \quad \nabla \cdot \mathbf{v} > 0, \quad (1)$$

where $\delta_{\text{tot}} \equiv \frac{\rho_{\text{tot}}}{\rho_B} - 1$ is the total density contrast. The threshold on the density gradient is set to $(\nabla \delta)^{\text{max}} = 0.25 \text{ Mpc}^{-1}$, in consistency with RQP13. Once the protovoid has been determined, the center of the void is adjusted to the center of mass defect of the protovoid. A first approximation to the shape of the ellipsoid is determined by computing and diagonalizing the inertia tensor.

Growth of the ellipsoidal void. The initial ellipsoid is subsequently grown iteratively to find the maximal ellipsoid that fits inside the actual void. This is performed by repeatedly applying the following two substeps:

1. The shape of the ellipsoid is adjusted iteratively, in a similar manner to what is done in the galaxy cluster’s literature (Zemp et al. 2011; Vallés-Pérez et al. 2020). In particular, the new eigenvalues of the inertia tensor yield the orientation of the void, while the new eigenvectors are

used to compute the new semiaxes. These semiaxes are rescaled proportionally, so as to preserve the volume of the ellipsoid. The process is iterated, adjusting the integration volume, until convergence, which is assessed by the change in the semiaxes lengths.

2. Once the shape has been found, the ellipsoidal void is grown at constant shape, by multiplying each of its semiaxes by a factor of $1 + \chi$. We have fixed $\chi = 0.05$, although this parameter does not have a severe impact on the resulting void population while kept small.

This two-step iteration is repeated until either one of the stopping conditions in RQP13 (maximum density, density gradient, or negative velocity divergence) is met by a cell, or the mean slope of the total density field at the boundary exceeds the prediction of the universal density profile (Ricciardelli et al. 2013, 2014b). It can be easily shown that, assuming that the spherical profiles in RQP13 can be extended to ellipsoidal shells, this condition can be applied by requiring:

$$3 \left(\frac{\rho(R)}{\rho(<R)} - 1 \right) > 1.37 - 0.25z, \quad (2)$$

with $\rho(<R)$ the mean density inside the ellipsoid and $\rho(R)$ computed from the newly added cells in the growing step. The numerical coefficients, which are derived from the fit in RQP13, are valid for $2.5 \geq z \geq 0$.

Void sample and merger tree. In order to produce the final sample of voids, we start from the latest code output (at $z = 0$) and select an initial sample of voids taking care of the overlaps. To do so, we iterate through the voids found by the algorithm described above, from the largest and emptiest to the smallest and densest, and accept those that do not overlap more than 50% with the volume occupied by previously accepted voids.

Then, we trace this initial sample back in time by building their merger tree. To assess which is the best progenitor candidate for a void, we find the one that maximizes the *volume retention* defined as $\text{VR} \equiv \frac{N_{A \cap B}}{\sqrt{N_A N_B}}$, with N referring to the number of cells, and A and B being some void and one of its parent candidates, respectively. This approach is equivalent to the *particle retention* defined by Minoguchi et al. (2021), but here applied to cells (Sutter et al. 2014). We did not find strong overall variations when using other figures of merit defined on Minoguchi et al. (2021), although there can be variations in a small number of individual voids.

With this procedure, we are able to obtain a sample of 207 voids, with equivalent radius at $z = 0$ larger than 5 Mpc (the largest of them reaching ~ 18 Mpc), which can be traced back, at least, to $z = 1.5$; and 179 of them are traced back down to $z = 2.5$. The overall statistics (radii, ellipticities, and mean overdensities) of the void sample are displayed in Figure A1.

2.3. The Pseudo-Lagrangian Approach and Its Validity

To assess mass fluxes in postprocessing, we take a pseudo-Lagrangian approach, by interpreting each volume element in the simulation (up to a certain refinement level) as a tracer particle, and advecting these tracer particles using the gas velocity field between each pair of code snapshots. This technique is analog to the one applied by Vallés-Pérez et al. (2020) for galaxy clusters.

In practical terms, at each code snapshot we take all (nonrefined and nonoverlapping) gas cells, each one at a

position \mathbf{x}_n and compute their updated position with an explicit, first-order step. For consistency, we have performed the same analysis with the dark matter particle distribution. Since voids experience mild dynamics with large dynamical times (associated to their low densities), this is a sensible approach. Then, in order to compute the accretion mass flux around a void between a pair of code outputs, we consider the mass of all the dark matter particles (or gas pseudo-particles) that were outside the void in the previous iteration, and inside the same volume at the latter (and vice versa for the decretion mass flux).

The previously discussed procedure will be valid as long as the timestep involved (the timespan between two consecutive outputs of the simulation) fulfills $\Delta t \lesssim \mathcal{L}/\mathcal{V}$, with \mathcal{L} a characteristic scale of the surface of the void, and \mathcal{V} a characteristic velocity for these cosmic flows. By choosing an ellipsoidal, instead of a complex, irregular shape, \mathcal{L} can be taken of the order of the smallest semiaxis (several Mpc). On the other hand, by using the same volume for both consecutive iterations, we ensure that we are detecting the mass elements that are being dynamically accreted onto the void, and not accounting for the elements that may appear inside or outside the ellipsoid due to its change between iterations.

We have also taken a conservative approach for the sake of showing the robustness of our results. Since DM particles can be traced, we can compare the total mass accretion in a certain redshift interval, when computed using our pseudo-Lagrangian method, and when computed by tracing the actual evolution of the particles in the simulation, i.e., checking which particles were outside the volume at the first iteration of the interval, and are inside that same volume at the last iteration. The results, shown in Figure A2, confirm that (i) the pseudo-Lagrangian approach works well, on a statistical level, on the DM particle distribution, with reasonable scatter (0.3–0.5 dex) between the estimated and the actual accretion inflow; and (ii) on these low-density environments, gas and DM dynamics exhibit remarkably similar results, producing a scatter between DM and gas accretion rates typically below 0.2 dex. This serves as a confirmation of the applicability of our pseudo-Lagrangian approach for estimating gas accretion.

3. Results

A summary of the results of this analysis over the whole cluster sample is shown in Figure 1, where we also present the decretion rates for comparison. The raw fluxes (gas or DM mass, entering or leaving the void per unit time) are displayed in the top panel, where it can be seen that accretion⁴ flows onto voids, while smaller in magnitude than the decretion flows typically by a factor of $1/6$ – $1/3$, are present in the void sample in a statistical sense.

In the middle panel we have normalized these fluxes to the mass of the given material component (gas or DM) in the void at each time, to be read as the percentage of gas or DM void’s mass that leaves or enters the void per gigayear. By performing this normalization, the robust mean values of the fluxes of DM and gas match each other, reflecting that both components undergo remarkably similar dynamics. This is expected, since gas in these regions has low temperature and pressure and thus

⁴ Although these mass inflows would not be triggered by the peculiar gravitational fields, but by the external, large-scale structure bulk and shear velocity flows, since they move inwards in the voids and remain within them for long times, we refer to them as accretion flows in analogy with mass flows in massive objects.

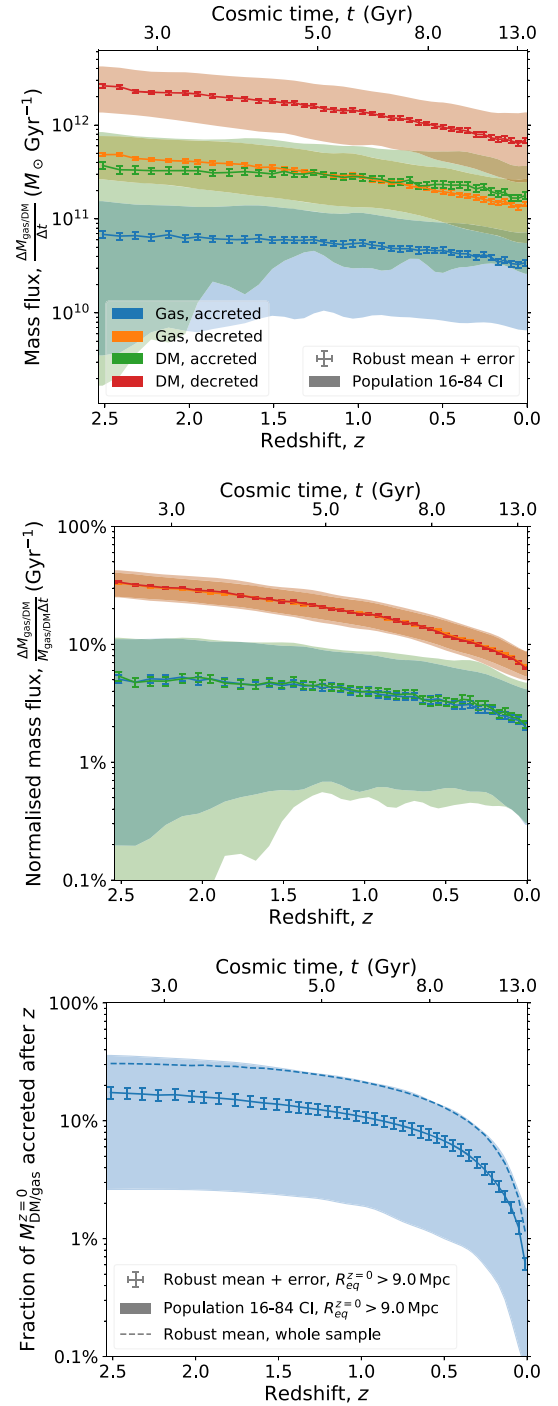


Figure 1. Evolution of the accretion and decretion rates in the void sample. Top panel: evolution of the mass fluxes (gas and DM mass, entering or leaving the void per unit time, according to the color legend) as a function of cosmic time. The shaded regions delineate the 16–84 percentiles (referred to as “confidence intervals” [CI] in the legend), as an indication of the scatter in these quantities, while the error bars represent the error of the mean value. Middle panel: mass fluxes normalized to the void’s gas or DM mass, averaged over the cluster sample. Same legend as above. Bottom panel: anticummulative gas mass fraction, i.e., the mass that has been accreted after a given redshift z as a fraction of the gas mass of the void at $z = 0$. Errors are given only for the $R_{\text{eq}}^{z=0} > 9$ Mpc for clarity, being similar in magnitude for the whole sample.

behaves closer to a collisionless fluid (further validating the applicability of the pseudo-Lagrangian approach; see Section 2.3). While normalized decretion flows show little

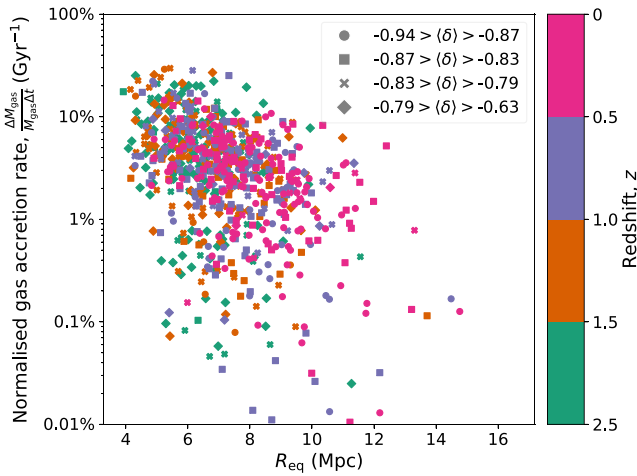


Figure 2. Normalized gas accretion rate, i.e., gas inflow per gigayear in units of the void’s gas mass (vertical axis) as a function of the size of the void (equivalent radius; horizontal axis). The gas accretion rates are computed on four redshift intervals, encoded in the figure according to the color scale on the right. The shapes of the data points refer to the mean overdensity of the void, according to the binning specified in the legend.

scatter, and evolve from nearly $30\% \text{Gyr}^{-1}$ at $z=2.5$ to $\sim 6\% \text{Gyr}^{-1}$ at $z \simeq 0$, accretion fluxes are smaller by a factor of $\sim 1/6$ at high redshift, but do not decrease as sharply and reach $\sim 1/3$ of the mean accretion values at $z=0$. It might be argued that part of these accretion flows could be due to void-in-cloud processes (Sheth & van de Weygaert 2004; Sutter et al. 2014, i.e., voids collapsing in a larger-scale overdense environment), even though our sample building strategy, from $z=0$ backwards in time, should exclude most of them since they would not have survived until $z=0$. Nevertheless, we have checked that the same results hold when restricting the sample to large voids ($R_{\text{eq}}^{z=0} > 9 \text{Mpc}$) only with a slight decrease in the accretion rates, less than a factor of 2, at low redshifts with respect to the whole sample. At high redshifts, there are no differences between large voids and the whole sample. Therefore, the accretion signal detected here cannot be ascribed to cloud-in-void processes alone. Smaller voids may experience stronger inflows, since they are more sensitive to external influences by a larger-scale velocity field.

Last, the bottom panel presents the accumulated accreted mass, as a function of the present-day void’s gas or DM mass, from a redshift z up to $z=0$. When focusing on the large-void subsample, on average, up to 17% of the void’s current mass has been accreted after $z=2.5$ (reaching beyond 35% at percentile 84), and the average void has suffered a mass inflow 10% of its current mass after $z=1$. Interestingly, in their general analysis of the cosmic web, Cautun et al. (2014) found that $\sim 20\%$ of the mass in voids at $z=0$ belonged to walls and filaments at $z=2$. Despite the similarity of the result, note that their interpretation is subtly different: while Cautun et al. (2014) ascribe this result to an artifact due to the difficulty of identifying tenuous structures within voids as they become emptier, our result corresponds to an actual inflow (matter initially outside the void, which crosses its boundary at a given time).

As the central result of this Letter, in Figure 2 we present the gas accretion rates (gas mass accreted, normalized by the voids’ mass and per unit time) as a function of the void size (equivalent radius), computed on four redshift intervals (from $z=2.5$ to $z=1.5$, and three subsequent intervals with

$\Delta z=0.5$ thereon) that are encoded by the color scale in the figure. A significant fraction of voids, at any redshift, presents relevant accretion rates (above a few percent per gigayear, which are sufficient to impact their composition and dynamics). The highest accretion rates are seen in the smallest voids. As mentioned above, smaller voids are more prone to externally induced flows due to larger-scale influences: while $R_{\text{eq}} \sim 5 \text{Mpc}$ voids show mean values $\sim 8\% \text{Gyr}^{-1}$, this rate lowers to $\sim (1-2)\% \text{Gyr}^{-1}$ in the case of the largest voids. Nevertheless, large voids with exceptionally large accretion rates also exist, even at low redshifts. Naturally, the abundance of small voids makes it possible for some of them to show extreme accretion rate values. The point markers encode the mean overdensity, $\langle \delta \rangle \equiv \langle \rho \rangle / \rho_B - 1$ of the voids, according to the legend, to check whether there is any trend between this property and the accretion rates. All voids in the sample, and even the large and rapidly accreting ones, have very small overdensities, thus ruling out the fact that our results could be contaminated by a bad delineation of the void’s wall. Indeed, as discussed in Section 2.2, our void identification technique has aimed to be conservative enough to exclude these possible effects.

To better visualize the effect, we show in Figure 3 the gas density field around a large void ($R_{\text{eq}} \simeq 12 \text{Mpc}$) with high accretion rates. Blue and green contours correspond to isodensity surfaces of $\rho/\rho_B \simeq 3$ and 0.5 , roughly enclosing mean total densities $15\rho_B$ and $4\rho_B$, respectively, in order to give context of the distribution of matter around the void. The orange shadow highlights the void, with mean total density $\rho/\rho_B \simeq 0.1$. On top, we overplot the accretion velocity field, that is, the velocity vectors in the region around the void where they point toward it. This representation clearly exemplifies the presence of coherent, large-scale streams of matter flowing toward cosmic voids from higher-density regions. Complementarily, in Figure A3 we show an animation of a gas density slice through a large ($R_{\text{eq}} \simeq 14 \text{Mpc}$) void that undergoes significant accretion, with the velocity field overplotted with arrows. The animation exemplifies the nature of these inflows: the velocity field around the void consists of its own induced outflow (dominant through most of its boundary), plus the bulk and shear flows originated by the surrounding structures (see also Aragon-Calvo & Szalay 2013 for a detailed study of the hierarchical nature of velocity fields in and around voids).

Tracing the newly accreted DM particles in time, we find that nearly 50% remain inside the original volume of the void for up to $\sim 10 \text{Gyr}$, and a significant fraction of them reach inner radii. The same behavior is expected for the gas, therefore granting the accreted gas, which may have been preprocessed outside the void, a long enough timespan to play a crucial role in the formation and evolution of void galaxies.

4. Conclusions

The findings reported in this Letter challenge the common accepted picture on the evolution of cosmic voids and could consequently have a direct potential impact on the understanding of galaxy formation and evolution in low-density environments. Hence, the uncontaminated and pristine void domains could be altered by the entrance of chemically and thermodynamically processed gas. Future effort should be devoted to confirm these results with other simulation codes and void identification strategies (e.g., those based on the

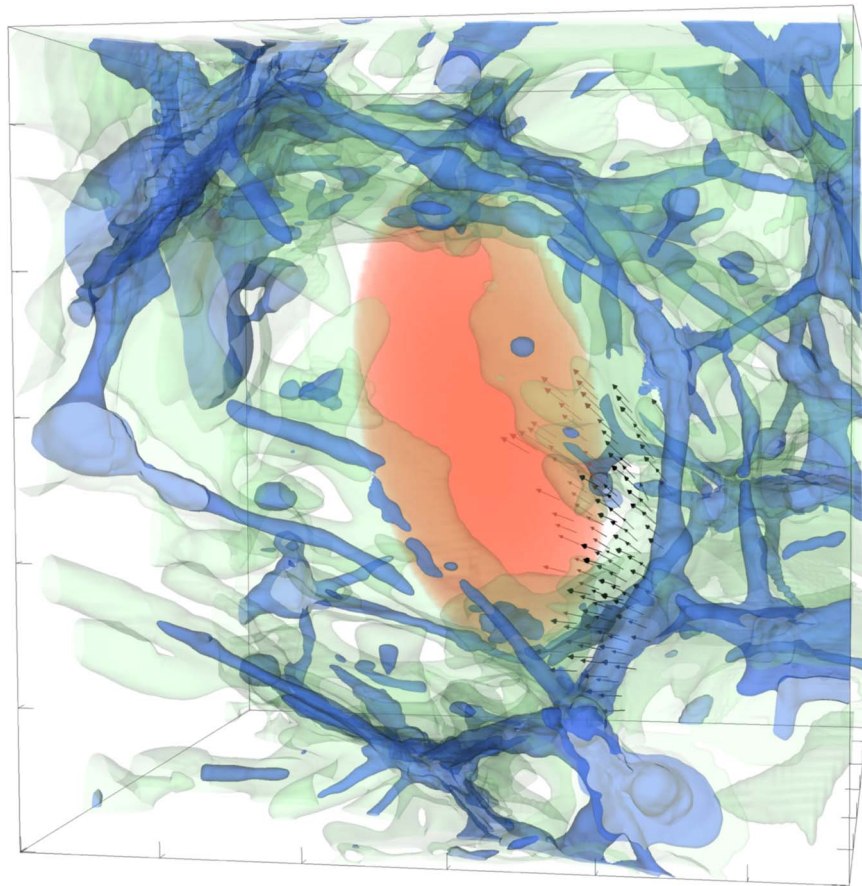


Figure 3. Close look at a large ($R_{\text{eq}} \simeq 12$ Mpc) void that undergoes significant accretion by redshift $z \simeq 0$. The box corresponds to a cubic domain ~ 56 Mpc (comoving) along each direction. The ticks on the axes are spaced 10 Mpc for visual reference. Blue and pale green contours represent the gas density, with blue and green regions approximately corresponding to collapsed (cluster and filaments) matter and diffuse gas around it, respectively. The orange, shaded area shows the location of the ellipsoidal void, which is well delineated by the surrounding matter. The arrows represent the gas velocity field around the surface of the void in those regions where gas is being accreted toward it.

watershed transform Platen et al. 2007; Neyrinck 2008; see, for example, the comparison project of Colberg et al. 2008).

The authors thank the referee for constructive criticism. This work has been supported by the Spanish Agencia Estatal de Investigación (AEI, grant PID2019-107427GB-C33) and by the Generalitat Valenciana (grant PROMETEO/2019/071). D.V. acknowledges partial support from Universitat de València through an *Atracció de Talent* fellowship. Simulations have been carried out using the supercomputer Lluís Vives at the Servei d'Informàtica of the Universitat de València.

Appendix Additional Material

This appendix contains three additional figures. Figure A1 presents a summary of the statistical properties of our void sample. Figure A2 presents the results on the checks of the robustness of the pseudo-Lagrangian approach (see Section 2.3). Finally, Figure A3 contains an animation displaying the evolution of a density slice with the velocity field overplotted, showing an example of mass inflows through void boundaries.

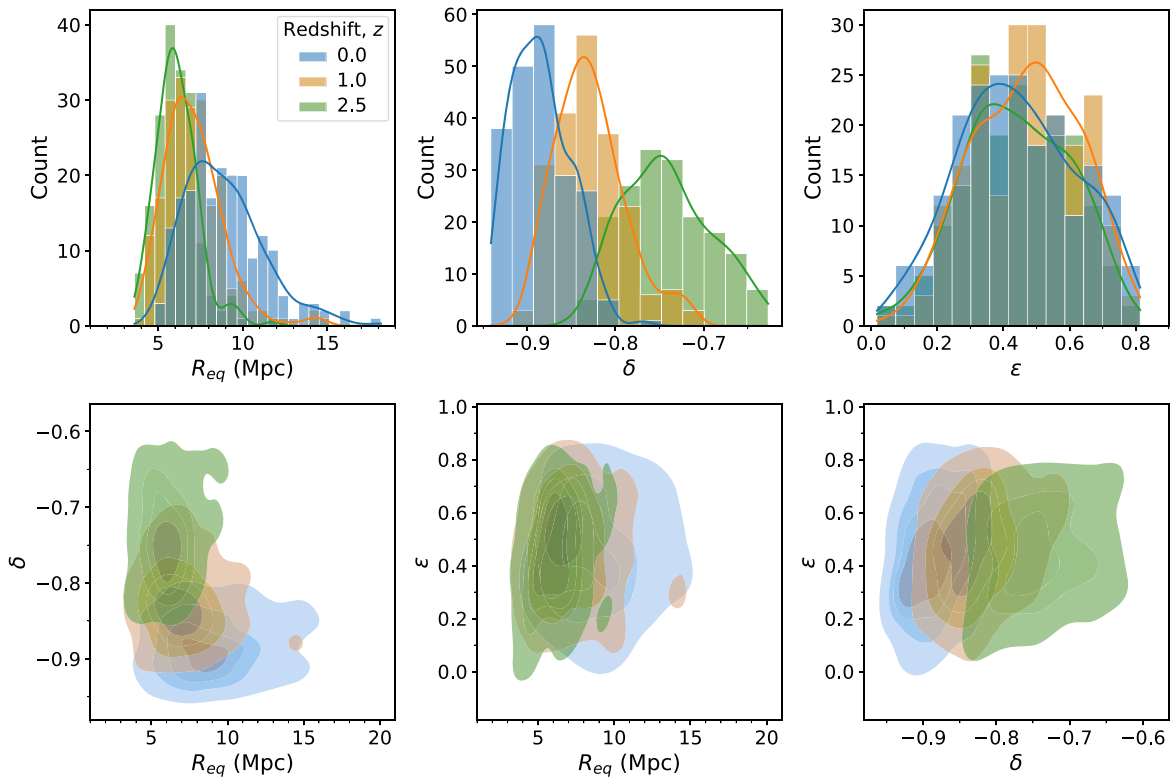


Figure A1. Summary of general properties of the void sample. Top row: distribution of the equivalent radius (R_{eq} , left panel), mean overdensity (δ , middle panel), and ellipticity (ϵ , right panel) for the voids sample at redshifts $z \approx 0$ (blue), 1 (orange), and 2.5 (green). Bottom row: joint distribution of each pair of variables, according to the same color palette. The continuous lines in the histograms, and the color contours in the joint distributions have been obtained by means of a Gaussian kernel density estimation procedure. Darker colors imply higher density of voids in the corresponding parametric space.

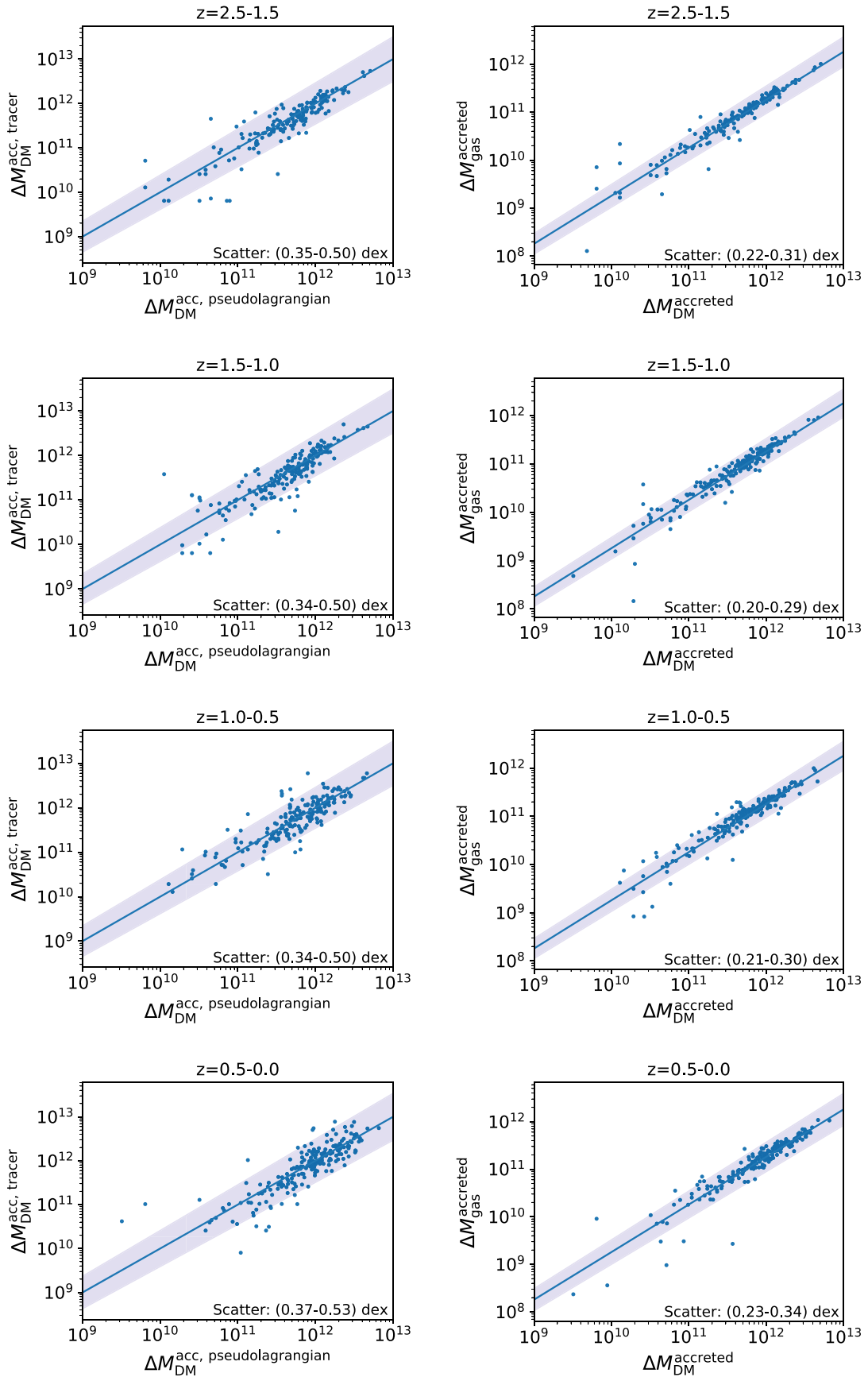


Figure A2. Left-hand column: correlation between the accreted DM mass computed according to our pseudo-Lagrangian method, and when computed by explicitly tracing DM particles in the simulation, in the redshift interval specified at the top of each panel. Right-hand column: tight correlation between the gas and the DM accreted mass, both computed according to our pseudo-Lagrangian algorithm.

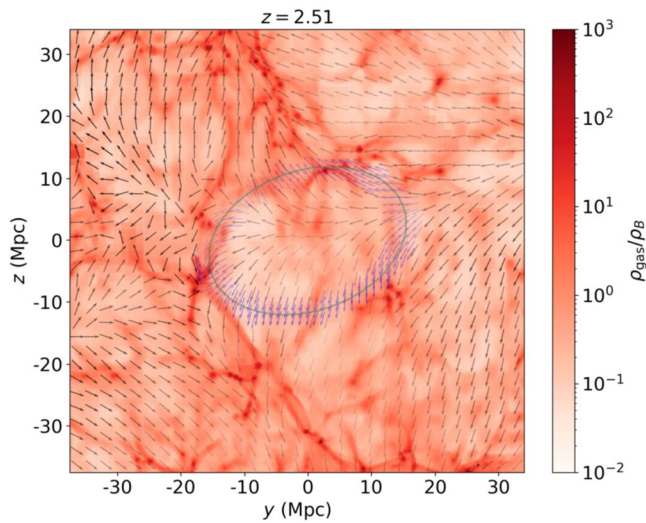


Figure A3. Animation showing the evolution of a density slice (~ 9 Mpc thick) through a large ($R_{\text{eq}} \simeq 14$ Mpc) void and its environment, from $z = 2.5$ to $z = 0$. The colors encode the gas density (in units of the background density) according to the adjacent color scale. The green ellipse represents the slice through the void's ellipsoid. Note that some part of the void's wall may appear to be inside the void due to projection effects. Nevertheless, the void overdensity is low, below $\langle \delta \rangle \sim -0.8$, thus ensuring that overdense regions are well excluded. Arrows represent the gas velocity field in the slice. Note that the size of the arrows is constant for better visualization, while the magnitude of the projected velocity vector is encoded in the opacity of the arrow (more opaque arrows imply higher velocity magnitudes). The velocity field around the void's boundary is sampled with higher density of arrows and colored blue for better visualization. Matter entering the void through its rightmost corner can be clearly visualized in the animation. This figure is available as an animation in the HTML version of the article. *Still frame:* first frame of the animation. *Duration:* 8 s.

(An animation of this figure is available.)

ORCID iDs

David Vallés-Pérez  <https://orcid.org/0000-0003-2656-5985>

Vicent Quilis  <https://orcid.org/0000-0002-2852-5031>

Susana Planelles  <https://orcid.org/0000-0002-0105-4815>

References

- Aragon-Calvo, M. A., & Szalay, A. S. 2013, *MNRAS*, 428, 3409
- Baushev, A. N. 2021, *MNRAS*, 504, L56
- Behroozi, P. S., Loeb, A., & Wechsler, R. H. 2013, *JCAP*, 2013, 019
- Bertschinger, E. 1985, *ApJS*, 58, 1
- Bos, E. G. P., van de Weygaert, R., Dolag, K., et al. 2012, *MNRAS*, 426, 440
- Bothun, G. D., Geller, M. J., Kurtz, M. J., Huchra, J. P., & Schild, R. E. 1992, *ApJ*, 395, 347
- Cautun, M., van de Weygaert, R., Jones, B. J. T., et al. 2014, *MNRAS*, 441, 2923
- Ceccarelli, L., Padilla, N. D., Valotto, C., & Lambas, D. G. 2006, *MNRAS*, 373, 1440
- Colberg, J. M., Pearce, F., Foster, C., et al. 2008, *MNRAS*, 387, 933
- Dekel, A., & Rees, M. J. 1994, *ApJL*, 422, L1
- Foster, C., & Nelson, L. A. 2009, *ApJ*, 699, 1252
- Hahn, O., Carollo, C. M., Porciani, C., & Dekel, A. 2007, *MNRAS*, 381, 41
- Kreckel, K., Platen, E., Aragón-Calvo, M. A., et al. 2011, *AJ*, 141, 4
- Lavaux, G., & Wandelt, B. D. 2010, *MNRAS*, 403, 1392
- Lavaux, G., & Wandelt, B. D. 2012, *ApJ*, 754, 109
- Minoguchi, M., Nishizawa, A. J., Takeuchi, T. T., & Sugiyama, N. 2021, *MNRAS*, 503, 2804
- Neyrinck, M. C. 2008, *MNRAS*, 386, 2101
- Padilla, N. D., Ceccarelli, L., & Lambas, D. G. 2005, *MNRAS*, 363, 977
- Park, D., & Lee, J. 2007, *PhRvL*, 98, 081301
- Patri, S. G., Betancort-Rijo, J., & Prada, F. 2012, *A&A*, 541, L4
- Paz, D., Lares, M., Ceccarelli, L., Padilla, N., & Lambas, D. G. 2013, *MNRAS*, 436, 3480
- Pisani, A., Massara, E., Spergel, D. N., et al. 2019, *BAAS*, 51, 40
- Planck Collaboration 2020, *A&A*, 641, A6
- Platen, E., van de Weygaert, R., & Jones, B. J. T. 2007, *MNRAS*, 380, 551
- Quilis, V. 2004, *MNRAS*, 352, 1426
- Quilis, V., Planelles, S., & Ricciardelli, E. 2017, *MNRAS*, 469, 80
- Ricciardelli, E., Cava, A., Varela, J., & Quilis, V. 2014a, *MNRAS*, 445, 4045
- Ricciardelli, E., Quilis, V., & Planelles, S. 2013, *MNRAS*, 434, 1192
- Ricciardelli, E., Quilis, V., & Varela, J. 2014b, *MNRAS*, 440, 601
- Sheth, R. K., & van de Weygaert, R. 2004, *MNRAS*, 350, 517
- Sutter, P. M., Elahi, P., Falck, B., et al. 2014, *MNRAS*, 445, 1235
- Vallés-Pérez, D., Planelles, S., & Quilis, V. 2020, *MNRAS*, 499, 2303
- van de Weygaert, R. 2016, *The Zeldovich Universe: Genesis and Growth of the Cosmic Web*, 308, 493
- van de Weygaert, R., & Platen, E. 2011, *IJMPS*, 1, 41
- van de Weygaert, R., & van Kampen, E. 1993, *MNRAS*, 263, 481
- Zeldovich, I. B., Einasto, J., & Shandarin, S. F. 1982, *Natur*, 300, 407
- Zeldovich, Y. B. 1970, *A&A*, 500, 13
- Zemp, M., Gnedin, O. Y., Gnedin, N. Y., & Kravtsov, A. V. 2011, *ApJS*, 197, 30
- Zhang, C., Churazov, E., Dolag, K., Forman, W. R., & Zhuravleva, I. 2020, *MNRAS*, 494, 4539